

PAPER • OPEN ACCESS

## Extending the low-recycling, flat temperature profile regime in the lithium tokamak experiment- $\beta$ (LTX- $\beta$ ) with ohmic and neutral beam heating

To cite this article: D.P. Boyle *et al* 2023 *Nucl. Fusion* **63** 056020

View the [article online](#) for updates and enhancements.

You may also like

- [Fusion applications for lithium: wall conditioning in magnetic confinement devices](#)

Robert Kaita

- [Oxidation of lithium plasma facing components and its effect on plasma performance in the lithium tokamak experiment-](#)

A Maan, D P Boyle, R Kaita et al.

- [VUV/XUV measurements of impurity emission in plasmas with liquid lithium surfaces on LTX](#)

Kevin Tritz, Ronald E Bell, Peter Beiersdorfer et al.

# Extending the low-recycling, flat temperature profile regime in the lithium tokamak experiment- $\beta$ (LTX- $\beta$ ) with ohmic and neutral beam heating

D.P. Boyle<sup>1,\*</sup>, J. Anderson<sup>2</sup>, S. Banerjee<sup>1</sup>, R.E. Bell<sup>1</sup>, W. Capecchi<sup>2</sup>, D.B. Elliott<sup>3</sup>, C. Hansen<sup>4</sup>, S. Kubota<sup>5</sup>, B.P. LeBlanc<sup>1</sup>, A. Maan<sup>1</sup>, R. Maingi<sup>1</sup>, R. Majeski<sup>1</sup>, J.E. Menard<sup>1</sup>, S. Oliva<sup>2</sup>, T. Rhodes<sup>5</sup>, V. Soukhanovskii<sup>6</sup> and L. Zakharov<sup>7</sup>

<sup>1</sup> Princeton Plasma Physics Laboratory, Princeton, NJ, 08543, United States of America

<sup>2</sup> University of Wisconsin, Madison, WI, 53706, United States of America

<sup>3</sup> Oak Ridge National Laboratory, Oak Ridge, TN, 37831, United States of America

<sup>4</sup> University of Washington, Seattle, WA, 98105, United States of America

<sup>5</sup> University of California at Los Angeles, Los Angeles, CA, 90095, United States of America

<sup>6</sup> Lawrence Livermore National Laboratory, Livermore, CA, 94550, United States of America

<sup>7</sup> LiWall Fusion, Princeton, NJ, 08543, United States of America

E-mail: [dboyle@pppl.gov](mailto:dboyle@pppl.gov)

Received 28 September 2022, revised 27 January 2023

Accepted for publication 16 March 2023

Published 5 April 2023



## Abstract

Recent experiments in the lithium tokamak experiment- $\beta$  (LTX- $\beta$ ) have extended the duration, performance, operating conditions, and diagnosis of the flat-temperature profile, low-recycling regime first observed in LTX. As expected, Li retains hydrogen and suppresses edge neutral cooling, allowing increased edge electron temperature, roughly equal to the core  $T_e$ . Flat temperature profiles had been obtained transiently in LTX, as the plasma density decayed following the cessation of edge gas puffing. Careful control over the fueling in LTX- $\beta$  has now been shown to sustain the flat  $T_e$  profile and hot edge unique to the low-recycling regime for multiple confinement times in high performance discharges with decaying or steady density. With low density, the flat  $T_e$  profile is also seen to extend into the scrape-off layer. Neutral beam heating is observed in target discharges with relatively flat electron temperature profiles ( $T_{\text{edge}} \sim T_{\text{core}}/2$ ), though beam heating is stronger in discharges with higher fueling, higher density, and depressed edge  $T_e$ . Beam heating produces additional peaking of the  $T_e$  profile, without degradation of the energy confinement time. Neutral beam heating of target discharges with relatively flat electron temperature profiles similarly results in broad beam heated temperature profiles. Energy confinement in LTX- $\beta$  generally compares favorably to ohmic and H-mode scalings, frequently exceeding them by factors of 2–4. New and improved diagnostics in LTX- $\beta$  enable better characterization of this unique regime, including measurements of ion temperature and high field side Thomson scattering profiles. As an initial step toward characterizing turbulence with no  $T_e$  gradient and roughly equal density and pressure gradient,

\* Author to whom any correspondence should be addressed.



Original content from this work may be used under the terms of the [Creative Commons Attribution 4.0 licence](#). Any further distribution of this work must maintain attribution to the author(s) and the title of the work, journal citation and DOI.

core fluctuation spectra have been measured in peaked  $T_e$  discharges using far-forward scattering and fluctuation reflectometry.

**Keywords:** low-recycling, lithium, tokamak, plasma–surface interactions, ohmic confinement, neutral beam injection

(Some figures may appear in colour only in the online journal)

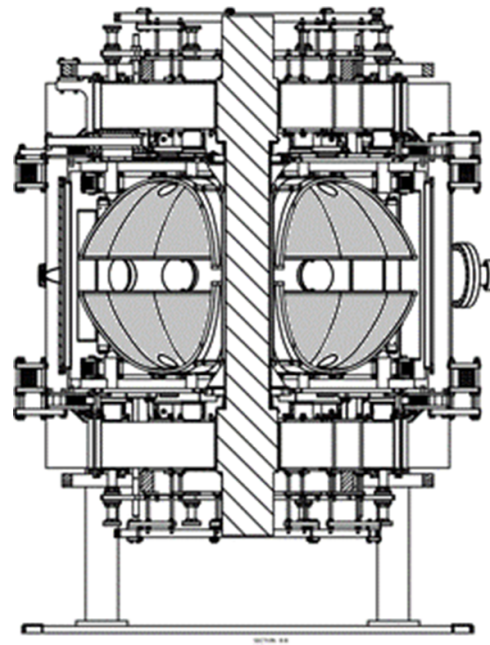
## 1. Introduction

The use of lithium coatings as a plasma facing surface has been observed to improve plasma performance in a number of fusion devices [1–13], and lithium as a liquid metal is a candidate for plasma facing components in fusion reactors [1, 2, 14]. While lithium has many potentially beneficial properties as a wall material, this work is mainly concerned with Li as a low-recycling surface. Li retains hydrogen isotopes, whereas most materials re-release virtually all incoming plasma ions as neutrals. Without a boundary condition of cold recycled gas, the plasma can develop a hot edge and a flat temperature profile with no gradient to drive transport or instabilities, potentially allowing improved confinement. This fundamentally different low-recycling regime has been long predicted [15–17] and was first demonstrated in the lithium tokamak experiment (LTX) [18, 19]. However, as strong edge gas fueling can also cause a cold boundary even with low-recycling surfaces, the initial observation was transient.

This paper describes new experiments in the upgraded LTX- $\beta$  to extend the duration, performance, operating conditions, and diagnosis of discharges with Li surfaces, especially the low-recycling regime. Section 2 describes the configuration of LTX- $\beta$  and the application of lithium to the plasma facing surfaces. Section 3 describes measurement and analysis of improved ohmic discharges, including low-recycling discharges, using Thomson scattering and TRANSP. Neutral beam heating and its effects on profiles and confinement are described in section 4. As changes to the temperature and density gradients are expected to impact turbulent fluctuations, far-forward scattering (FFS) and fluctuation reflectometry measurements are described in section 5. Section 6 summarizes and discusses these results and future plans for LTX- $\beta$ .

## 2. Configuration

The LTX- $\beta$  is a low aspect ratio tokamak with major radius  $R_0 \sim 0.4$  m, minor radius  $a < 0.26$  m, and elongation  $\kappa \sim 1.5$  [20, 21]. Typical parameters are toroidal field  $B_T \sim 3$  kG, plasma current  $I_P < 140$  kA (100–120 kA in the discharges considered here), and a discharge duration  $\sim 50$  ms. LTX- $\beta$  has retained the 1 cm thick copper shell used in LTX [22, 23], which approximately conforms to a flux surface for a full-volume plasma. The shell is divided into four quadrants and the plasma-facing surface is clad with explosively bonded 1.5 mm thick 304 stainless-steel. Prior to a day's operations, the stainless-steel cladding can be evaporatively coated with lithium to form the plasma-facing surface. An elevation



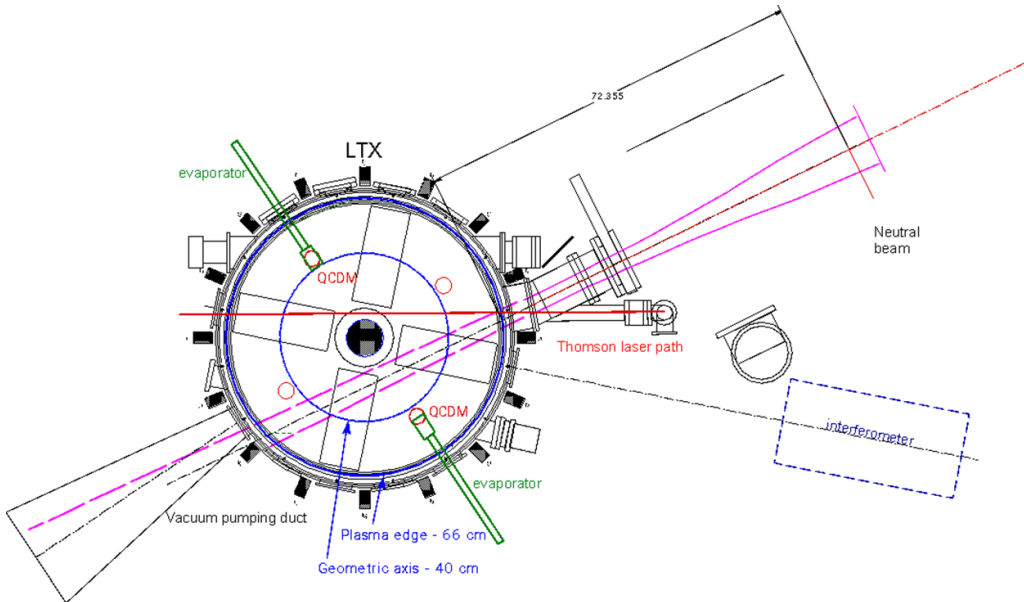
**Figure 1.** Elevation of LTX- $\beta$ . The upper and lower shells, which are coated with lithium, are shown in gray on the interior of the vacuum vessel. The shells are suspended within the vacuum vessel to allow for thermal expansion when heated to 350 °C. Not shown are the two toroidal gaps in the shells, located 180° toroidally apart.

diagram of LTX- $\beta$  is shown in figure 1 while a top-view layout of LTX- $\beta$  is shown in figure 2.

The shell covers 80% of the plasma surface area and can be electrically heated to 350 °C to liquefy the lithium coatings, although the results presented here were obtained with solid coatings. For the results presented here, the shells have been repeatedly coated with lithium over a period of 3–4 years, so that without continuous fueling, rapid density pumpout is always observed, and high recycling discharges can no longer be obtained [24]. LTX- $\beta$  is typically limited on the high field side (HFS) shell surfaces, at a radius of  $R = 14$  cm at midplane. The outer shell surface maps to  $R = 66$  cm at the low field side midplane.

### 2.1. Lithium evaporators

The system of evaporators which are used to provide lithium wall coatings is described by Maan *et al* [24], and the toroidal positions of the two evaporators, when fully inserted into the torus, are shown in figure 2. During initial operation of the evaporator, part of the lithium evaporant dripped from the



**Figure 2.** LTX- $\beta$ , showing the neutral beam (see section 4) and locations of the lithium evaporators. The tangency radius for the beam is  $R = 24$  cm, well to the HFS of the plasma axis. The ports labeled ‘QCDM’ note the locations of the quartz crystal deposition monitors, above the lithium evaporators.

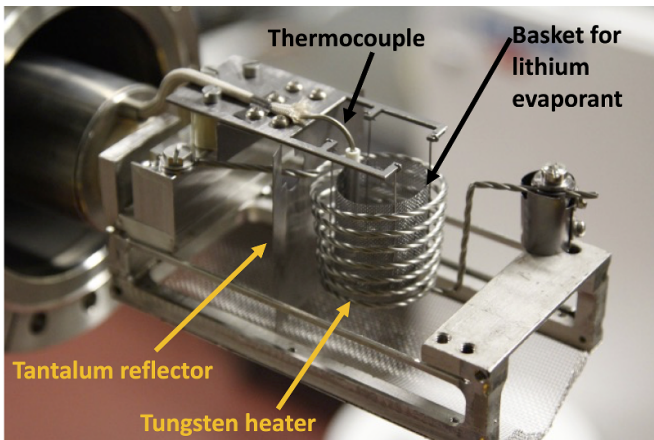


**Figure 3.** Lithium evaporator. Two bellows-mounted evaporators produce complete coverage of the stainless-steel plasma-facing shell surfaces with lithium. The tantalum reflector is heated by proximity to the tungsten heater and re-evaporates lithium toward the HFS surfaces of the shells, where the plasma is limited.

bottom of the woven tantalum mesh basket, shown in figure 3. Although lithium was found to wet the woven tantalum basket well, wicking through the woven material resulted in the formation of a pendant drop under the basket, which was prone to dripping.

Dripping was eliminated with the installation of a felt-metal liner for the basket, constructed from 60-micron 316L stainless-steel filtration media. Pendant drops are not formed on the bottom of the felt-metal liner. The bellows-mounted evaporator head is shown in figure 3, prior to installation on LTX- $\beta$ . QCDM are located above the positions of the fully inserted evaporators in order to monitor the thickness of the lithium films. A model of the evaporator has been developed

to use this single location to benchmark the film thickness, and project coating thickness over the entire shell inner surface.

### 3. Ohmic discharges

#### 3.1. Sustained flat temperature profiles with steady or decaying density

One of the key results from the LTX experiment was the demonstration that the electron temperature profile in a tokamak could be flat, rather than centrally peaked, if recycling is sufficiently low [18, 19]. However, the only well-diagnosed LTX flat temperature profiles were obtained transiently, following the cessation of gas puffing, as the neutral fueling gas pressure decayed. In experiments on LTX- $\beta$ , careful control over gas fueling has produced discharges with sustained flat temperature profiles.

Even before flat temperature profiles were obtained in LTX, the importance of efficient core fueling, so as not to simply replace recycling with a similar low-efficiency neutral source that equally cools the edge, was recognized by theory [15–17] and motivated early LTX experiments. Initial fueling studies investigated a relatively distant and undirected puffer, a more close-coupled directed tube, a re-entrant supersonic gas injector (SGI), and a molecular-cluster injector, all on the low-field side [25]. Finally, a HFS injector was used for the flat temperature profile results. In LTX- $\beta$ , the high-field side injector was modified and provides good performance but cannot be shut off quickly. The SGI can be shut off in a fraction of a ms and has been moved to the top of the vessel where it is inserted vertically through a shell penetration at  $R = 44.5$  cm. Waveforms from example discharges using HFS fueling for steady density and SGI fueling for decaying density are shown in figure 4.

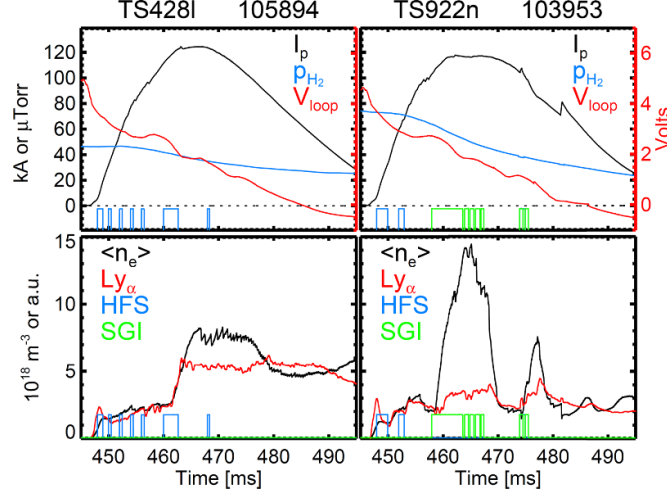


**Figure 4.** Discharge waveforms showing steady density with HFS fueling (left) and decaying density with SGI fueling (right). Top panels show plasma current (black) and neutral pressure (blue) on left axes and loop voltage (red) on right axes. Bottom panels show line-averaged density (black), Lyman- $\alpha$  emission on radial midplane [24] (red), and gate pulses for HFS fueling (blue) and SGI fueling (green).

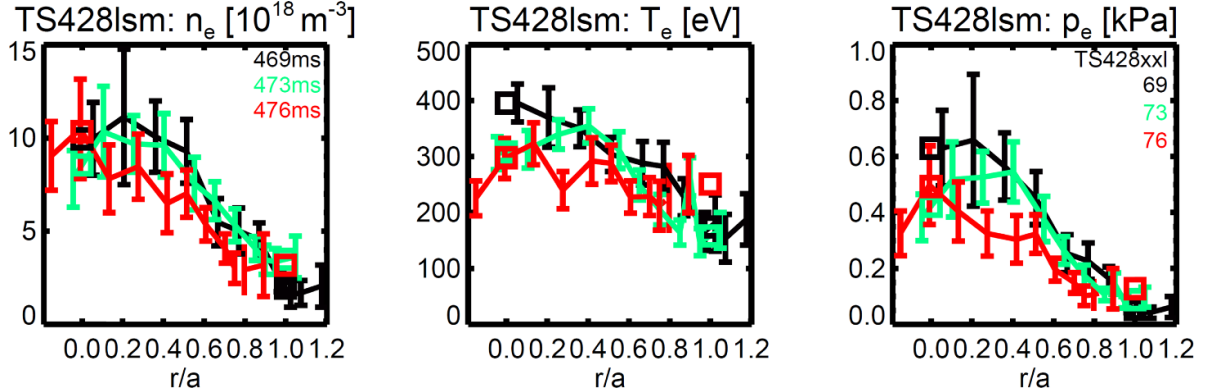


**Figure 5.** Relatively flat temperature profiles ( $T_{\text{edge}} \sim T_{\text{core}}/2$ ) with a hot edge are observed to remain for several milliseconds, even with continuous fueling to maintain roughly constant density in LTX- $\beta$ .

Thomson scattering profiles from an ensemble of repeated discharges that used a modest gas pulse from the HFS injector to achieve relatively steady and flat  $T_e$  profiles are shown in figure 5. While a quantitative understanding of the profiles and neutrals requires additional analysis [26], for the present we theorize that a low-density edge allows sufficient neutral penetration for core fueling while electron cooling from neutrals and ions is not excessive in the hot, low-collisionality edge. Note that both fueling efficiency and core penetration are higher with directed HFS puffing than with recycling.

In figure 6, a discharge with rapid density decay following termination of a large SGI puff is shown. Here, the Thomson scattering data extends into the scrape-off layer (SOL); the last closed flux surface (LCFS) and magnetic axis from equilibrium reconstructions are shown in the contour plots as black and white dashed lines. Electron temperatures in the SOL become comparable to the core values, after the central density drops to  $\sim 10^{19} \text{ m}^{-3}$ . Since Thomson scattering on LTX- $\beta$  employs a single-pulse ruby laser, it is necessary to scan the laser firing time through repeated discharges in order to obtain a temporal evolution of temperature and density profiles. In

addition, the data from Thomson scattering is averaged over several discharges, so the data shown in figure 6, and in all similar figures in this paper, is representative of a large ensemble of discharges.

Time dependent TRANSP analyses for the discharges shown in figure 6 are shown in figure 7.

TRANSP is a 1.5D equilibrium and transport solver for interpretation and prediction of tokamak discharges [27, 28], and is used here in a similar way to [18, 29]. TRANSP evolves the magnetic diffusion equations to match  $I_p$ ,  $B_T$ , and  $V_{\text{loop}}$  from magnetic measurements,  $n_e L$  from the interferometer, equilibrium reconstructions from PSI-Tri, and  $n_e$  and  $T_e$  profiles from Thomson scattering (with constant profile shapes extrapolated beyond the TS measurement window), with all data averaged over the ensemble of repeated shots. This TRANSP analysis assumes a fixed  $Z_{\text{eff}} = 1.3$  due solely to Li, but none of the conclusions are strongly dependent on this assumption. Previous studies in LTX and CDX-U using similarly extensive Li coatings found low  $Z_{\text{eff}} < 1.3$  using bolometry and by measuring/modeling profiles of the most important impurity species, Li, C, and O [29].

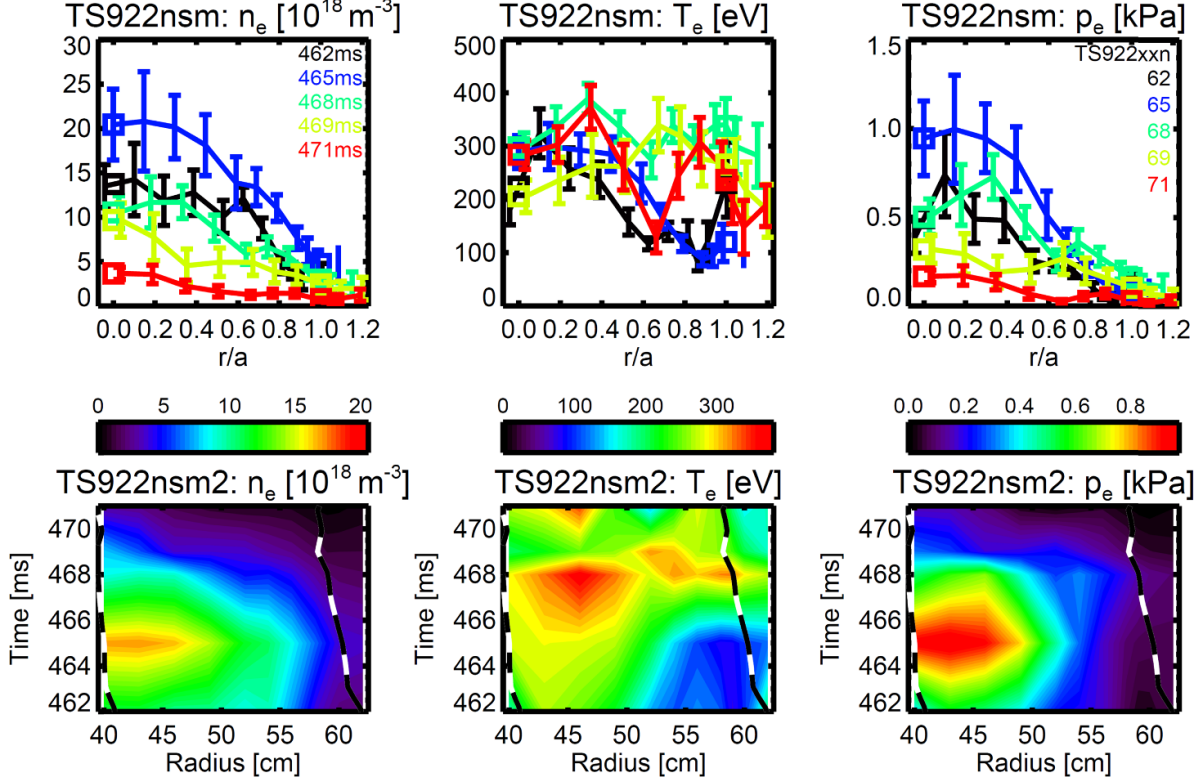


**Figure 6.** Flattening of the electron temperature profile is consistently observed with lithium coated walls, in the interval following a gas puff. Here flat temperature profiles persist for several milliseconds. In this case flat temperatures are observed into the scrape-off layer, past the last closed flux surface (dashed lines in contour plots) at  $R \sim 60 \text{ cm}$ .

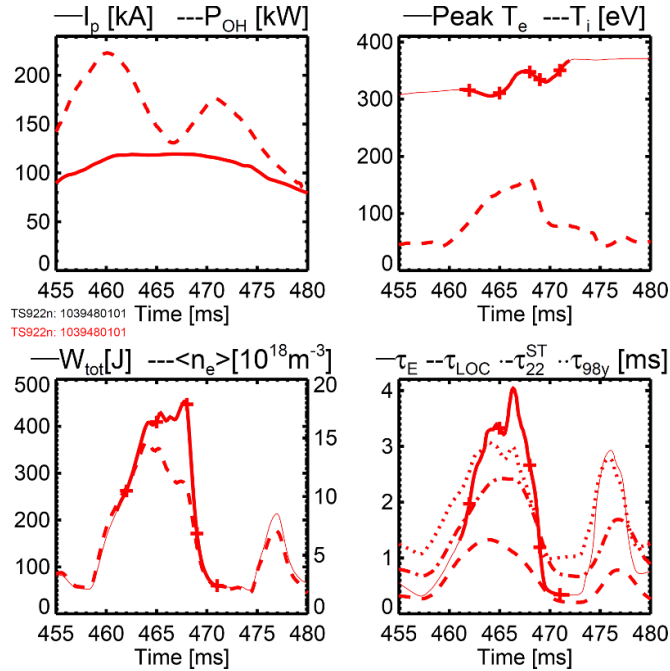


**Figure 7.** TRANSP modeling for the discharges shown in figure 6. Plots show plasma current  $I_p$  and modeled Ohmic heating power  $P_{OH}$ ; peak values of electron and ion temperature  $T_e$  and  $T_i$ ; stored energy  $W_{tot}$  and line-averaged density  $\langle n_e \rangle$ ; energy confinement time as modeled  $\tau_E$  and as predicted with ohmic scaling  $\tau_{LOC}$ , H-mode scaling  $\tau_{98y}$ , and spherical tokamak (ST) H-mode scaling  $\tau_{22}^{ST}$ . Times of Thomson scattering measurements are shown as + signs on thick lines in the  $T_e$ ,  $W_{tot}$ , and  $\tau_E$  plots, while unconstrained extrapolations by TRANSP are shown as thin lines.

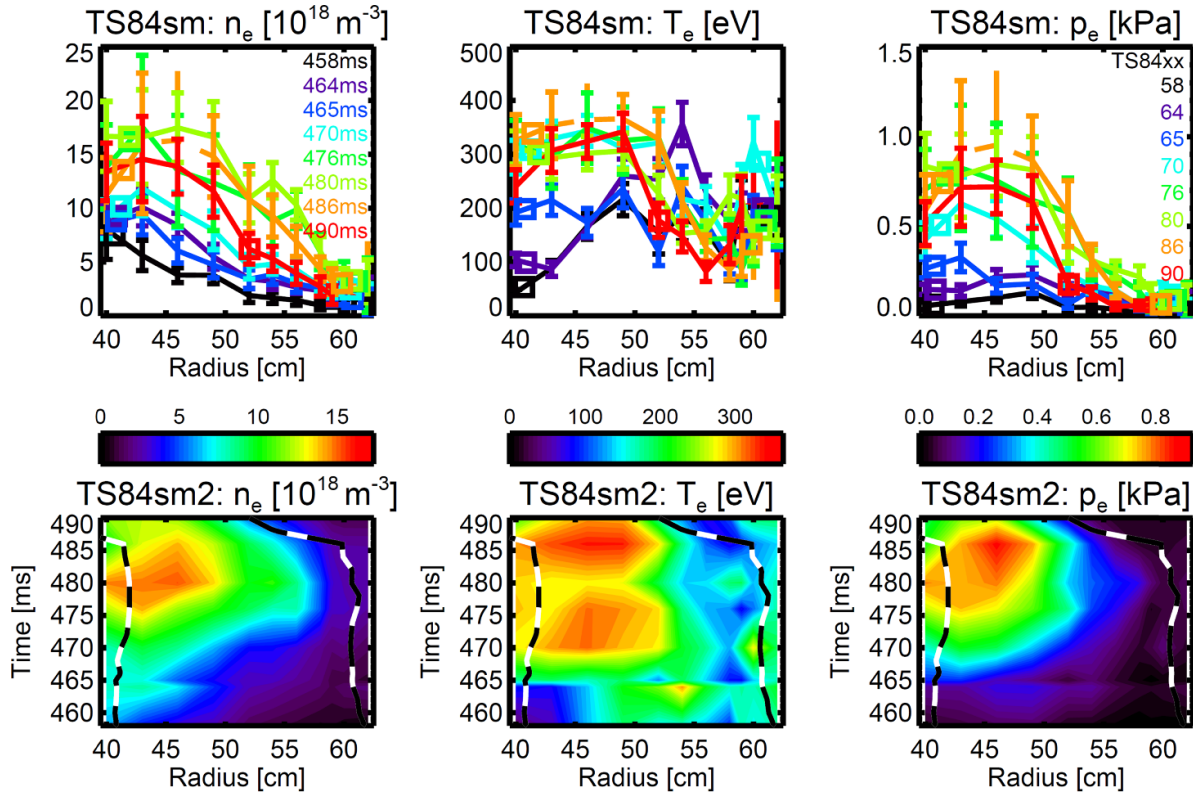


**Figure 8.** Evolution of the electron density and temperature from an ensemble of discharges with an extended current flattop, with lithium plasma facing surfaces. Squares or dashed black and white lines indicate the position of the axis and the low field side last closed flux surface.

The 3–4 ms peak energy confinement time from TRANSP modeling is  $\sim 3 \times$  neo-Alcator Linear Ohmic Confinement scaling (LOC) [30, 31], which is the appropriate comparison for an ohmic discharge. As LTX- $\beta$  does not have a divertor and plasmas are generally limited on the high-field side shell surfaces, it does not operate in H-mode. Nonetheless, energy confinement compares favorably to both the ITER H98y scaling [31] and the Globus-M2 ST H-mode scaling (ST22) [32, 33]. The data was taken with two fresh lithium evaporation, one before the start of tokamak operations (100 nm of lithium), and the other midway through the run day (50 nm of lithium), for a total evaporated mass of 0.86 g. To estimate recycling, hydrogen neutral flux from the wall was measured using a hydrogen Lyman-alpha array [24], and hydrogen ion fluxes to the walls were calculated using a simple, scaled 1D sheath limited model [34, 35]. In comparison to older Li coatings that are expected to have a higher recycling coefficient, these discharges with fresh lithium surfaces had a DEGAS2 [36] modeled recycling coefficient close to 0.5 [35].

For these ohmic plasmas, the ion temperatures were modeled by TRANSP assuming neoclassical ion confinement. The discharges used for this analysis were rapidly evolving, in part because the plasma current is not feedback controlled, and also because fueling was provided by a combination of the HFS gas puffing system and the SGI [24, 25]. The SGI produces a fast rising, fast falling fueling gas pulse which, in a tokamak with low recycling walls, produces a corresponding fast response in the plasma

density. The rapidly evolving nature of the discharges requires that a time-dependent TRANSP analysis be performed and produces a time-dependent estimate for the confinement time.

### 3.2. Extended current flattop duration

Recently, the control software for the ohmic power supply was upgraded, enabling discharges with long current flattops that exhibit steady increases in confinement time. Electron density, temperature, and pressure from a set of discharges with a long current flattop and a moderate plasma density are shown in figure 8. Prior to operations, a nominal 100 nm coating of fresh lithium was evaporated onto the shells.

The electron temperature profile is hollow at the start of the  $I_p$  flattop, then flattens and evolves to a broadly peaked  $T_e$  profile, with edge temperatures remaining in the 100–200 eV range through the data record. Note that the plasma edge moves inward to  $R \sim 53$  cm at the end of the current flattop. The density rises moderately through the  $I_p$  flattop.

At higher densities the duration of the current flattop is reduced. Figure 9 displays data from a more heavily fueled, higher density version of the discharge shown in figure 8. The peak electron density is increased from  $< 2 \times 10^{19} \text{ m}^{-3}$  to  $\sim 4 \times 10^{19} \text{ m}^{-3}$ , and the contour plots show that peaking of the density profile increases. The central electron temperature is reduced at higher density, but the electron pressure peak increases overall.

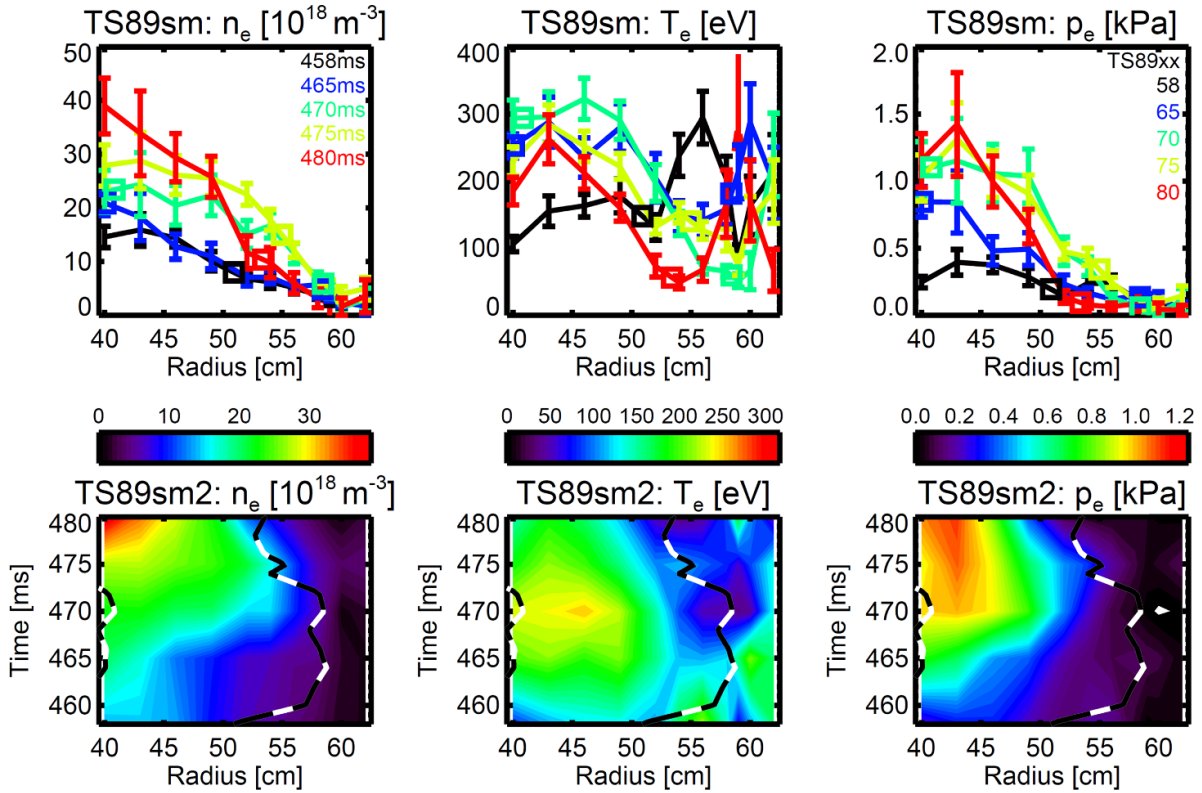


**Figure 9.** Evolution of the electron density and temperature from an ensemble of discharges with an extended current flattop, lithium plasma facing surfaces, and increased density compared to the discharge displayed in figure 8. Squares or dashed black and white lines indicate the position of the axis and the low field side last closed flux surface.

The TRANSP analysis for both sets of discharges is shown in figure 10. The ion temperature in these ohmic discharges is not experimentally measured, but rather calculated by TRANSP assuming neoclassical ion confinement. Electron temperature, stored energy, and confinement time rise through the current flattop. In both the low and high density cases, the peak confinement times are  $\sim 3\text{--}4 \times \text{LOC}$  and  $\sim 2 \times \text{H98y}$  and ST22 confinement scalings [30–33]. The stored energy shown in figure 10 is derived from the measured electron temperature and a TRANSP estimate of the ion temperature, assuming neoclassical ion transport.

Although direct measurement of the ion temperature was not available for these discharges, stored energy is also estimated from PSI-Tri [37] magnetic equilibrium reconstructions using a corrected diamagnetic loop. A significant number of corrections are required to obtain the stored energy from the magnetic measurement in LTX- $\beta$ , due to large, rapidly-evolving eddy currents and compression of various field components between the plasma and the stainless-steel-faced copper shell. For these discharges, with a longer plasma current flat top, the magnetic and the kinetic estimates of the stored energy agree for the latter part of the discharge, after the initial current ramp, as shown in figure 10.

#### 4. Neutral beam heated discharges

The upgrade of LTX to LTX- $\beta$  included the installation of a short-pulse neutral beam (10–20 keV, up to 35 A injected

H neutrals) [20, 38, 39]. The available port geometry on the vacuum vessel (see figure 2) limited the range of tangency radius for neutral beam injection (NBI). Initially, the beam was installed with a tangency radius of  $R = 19$  cm, with the option of re-aiming the beam to larger radius ( $R = 27$  cm) by swiveling the source on its bellows mount. Over this range, operation at a smaller tangency radius produces a larger population of fast ion first orbit losses, according to modeling with a full ion orbit code [40]. When the beam source is oriented at the largest available tangency radius, part of the beam footprint is blocked by the vacuum vessel port. For this work, an intermediate tangency radius of  $R = 24$  cm was chosen. Operation at this tangency radius does not eliminate first orbit fast ion losses, so that injection at reduced energy ( $\sim 13$  keV) is also employed to reduce losses, although at the expense of reducing heating power. Operation at lower injection energy also reduces beam shine-through. However, since the neutral beam is optimized for operation at 17–20 keV, the extracted current and total power from the beam is significantly reduced at lower acceleration voltages.

##### 4.1. NBI heating with relatively peaked $T_e$ profiles

Figure 11 presents a summary of TRANSP analysis, with the neutral beam heating analysis package NUBEAM [41], for a relatively peaked  $T_e$  profile discharge with neutral beam heating in LTX- $\beta$ , compared to an otherwise identical ohmic discharge. In this analysis, neoclassical ion transport coefficients

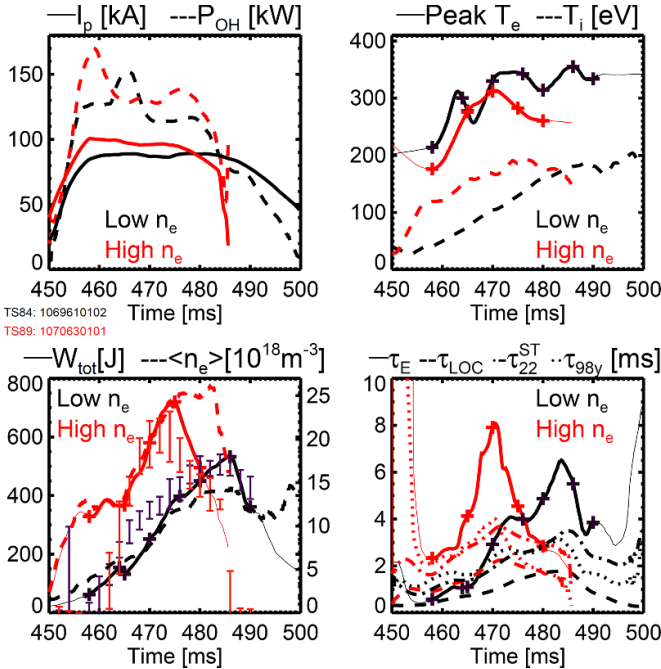


**Figure 10.** TRANSP analysis for the discharges with extended current flattops shown in figures 8 and 9. Stored energy from magnetics only reconstructions is shown with error bars representing the standard deviation of measurements from the ensembles of repeated shots. The ohmic loop voltage is maintained at approximately 1 V to maintain the flattop in the low-density case, and ~10% higher in the high-density case.

are scaled by TRANSP so the core ion temperature matches peak  $T_i$  measurements from C VI spectroscopy (see below). The injected neutral beam power was 310 kW with <20 kW of shine through. Direct losses of fast ions to the shell structure, from NUBEAM modeling, is significant; up to 70 kW, with some additional losses due to charge exchange. As a result, the combined ohmic and coupled neutral beam power is approximately 400 kW, compared to ~260 kW of ohmic heating in the comparison discharge. For NBI at low energy, with a target electron temperature of 150–250 eV, beam coupling is dominated by charge exchange, and the injected fast ions slow down primarily on the plasma electrons. The slowing down time on electrons  $\tau_{se}$  ranges from a few to >10 ms, varying as  $T_e^{3/2}/n_e$ . Since the beam duration is 5–8 ms, tests of beam heating at present are limited to relatively cold, dense target plasmas.

The peak ion temperature (upper right panel in figure 11, measurements from C VI shown with error bars) indicates that ion heating during beam injection is small (mainly seen at 472 ms), but the electron temperature increases in the neutral beam heated discharge compared to the ohmically heated comparison discharge. The stored energy during the beam pulse is approximately doubled in the beam heated discharge, while the confinement time is similar for both the ohmic and beam heated discharges.

Electron density, temperature, and pressure profiles for the discharges compared in figure 11 are shown in figure 12, for the time of peak measured electron heating (471 ms). Beam

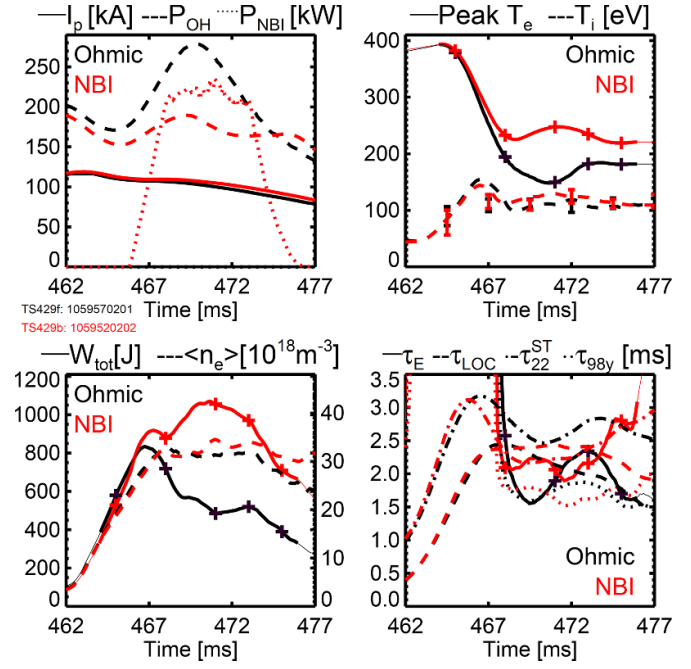
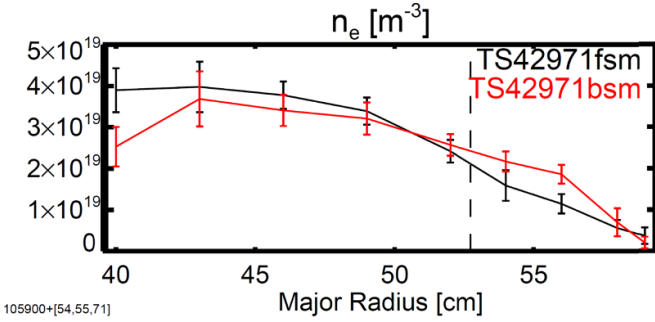


**Figure 11.** TRANSP and NUBEAM analysis of high-density discharges with low energy (13 keV) NBI (red), and comparable ohmic discharges (black). Peak injected neutral beam power was ~350 kW; the power  $P_{NBI}$  indicated in the upper left panel (dotted line) is beam power coupled to the plasma. The drop in peak electron temperature shown in the upper right panel is a consequence of strong fueling, just prior to beam injection, to increase the target plasma density. Modeled ion temperature is constrained to match measurements from C VI line broadening.

shine through at this time is calculated to be <2.5%, peaking at ~5 kW. This is the estimate produced with NUBEAM modeling with TRANSP; a direct measure of beam shine through is not available on LTX- $\beta$ . The electron temperature is not flat, since strong gas puffing was employed to produce a high target density. Strong puffing also reduces the target electron temperature, and therefore the slowing down time of the fast injected ions, to a few milliseconds, so that the fast ion slowing down time on electrons  $\tau_{se}$  is shorter than the modest beam pulse length of ~7 ms. Unfortunately, this present restriction limits effective beam heating to lower electron temperature discharges in LTX- $\beta$ .

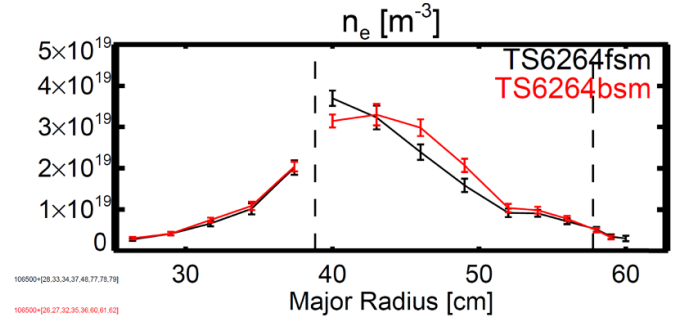
#### 4.2. NBI heating with relatively flat $T_e$ profiles

Although discharges with flat temperature profiles are now routinely obtained in LTX- $\beta$ , such discharges typically require reduced gas fueling, so that plasma density is lower and electron temperature higher than the other discharges used as neutral beam targets (figures 11 and 12). Rapid fueling during the current ramp can achieve moderately dense, cool, and flat temperature profiles, though the plasmas tend to be more unstable and shorter lived than discharges with more gradual fueling. Beam shine-through is larger, fast ion losses to the surrounding shells are larger, and the fast ion slowing down times are comparable to or longer than the beam pulse length. Under these



105900+[54,55,71]

105900+[52,53]



106500+[28,33,34,37,48,77,78,79]

106500+[28,27,32,35,36,60,61,62]

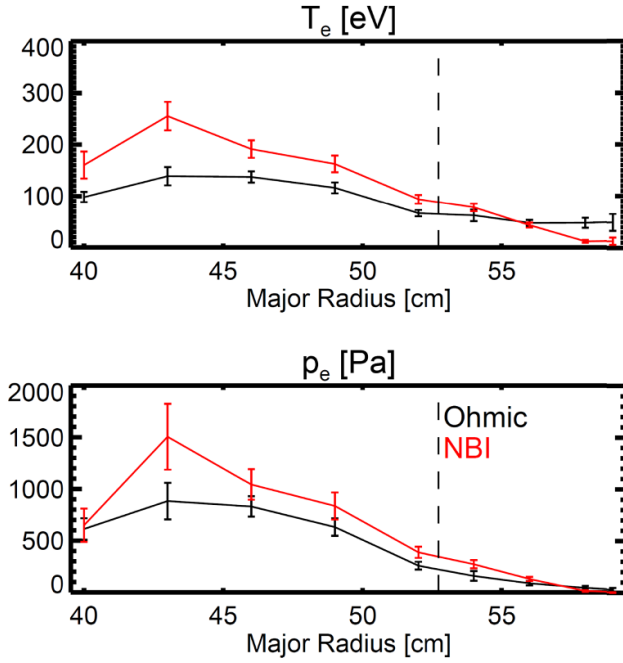


**Figure 12.** Thomson scattering radial profiles of electron density, temperature, and pressure at 471 ms for discharges in figure 11 with low energy NBI (red), and comparable ohmic discharges (black).

conditions, neutral beam heating is weaker than for denser, colder targets.

A comparison of the electron temperature, density, and pressure profiles for relatively flat temperature discharges ( $T_{\text{edge}} \sim T_{\text{core}}/2$ ) with and without NBI is shown in figure 13, which can be compared with the results for denser, colder discharges with peaked electron temperatures in figure 12. These profiles incorporate measurements from the new five channel polychromator-based high field side Thomson scattering (HFSTS) [42], though it should be noted the HFSTS density profile is presently uncalibrated, and some channels are rescaled empirically to account for apparent viewing aperture clipping of the scattered laser light. The line-integrated density measured with interferometry is used as a constraint to normalize the density profile. The HFSTS data confirms the relatively flat temperature profile extends across the magnetic axis and is modestly hotter with the addition of NBI.

In order to determine ion temperatures, spectra from multiple species were measured with a high-throughput spectrometer with a fiber array [43] along twelve sightlines viewing away from the neutral beam path. The measured passive

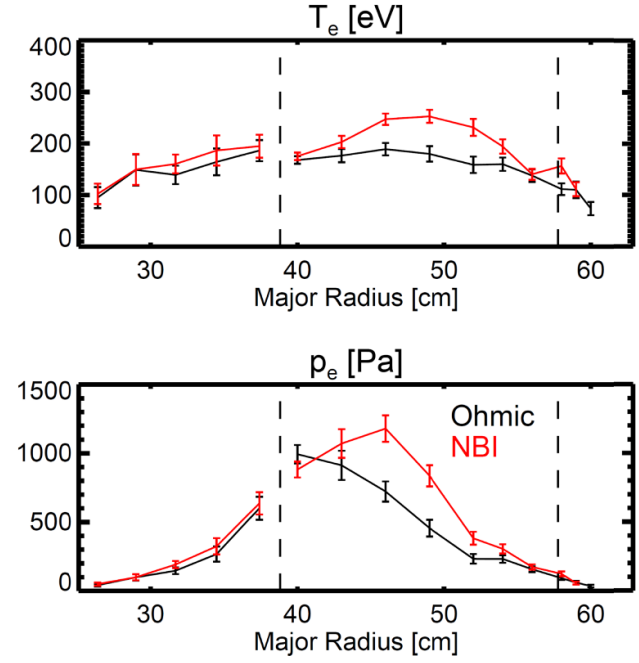


**Figure 13.** Thomson scattering radial profiles of electron density, temperature, and pressure during beam heating of discharges with relatively flat temperature profiles ( $T_{\text{edge}} \sim T_{\text{core}}/2$ ). Heating is less pronounced than for discharges with denser, colder plasmas.

emission from the C III triplet near 465 nm, the Li III line at 450 nm, and the C VI line at 529 nm were used to reconstruct an ion temperature profile using multiple matched plasma discharges. A matrix inversion technique [44] was used to obtain local values of emissivity and ion temperature from the line-integrated measurements. In figure 14, the line-integrated ‘apparent’ ion temperatures (points with error bars), as well as the inverted local temperature profiles (splines with error bands) are shown along with the relatively flat electron temperature profiles (red) from the ohmic and NBI-heated discharges in figure 13. Figure 14 shows that while edge  $T_e$  is high, edge  $T_i$  from C III can remain low, likely due to charge exchange losses during the edge fueling found to be necessary for beam coupling. In the core, calculated uncertainty in the inversion of  $T_i$  is high, though the close agreement between the Li III and C VI inverted and line-integrated  $T_i$ , as well as consideration of the Thomson and emissivity profiles, gives reasonable confidence in using the peak line-integrated  $T_i$  measurements to constrain TRANSP simulations. The various  $T_i$  measurements also agree in showing a modest  $T_i$  increase in the NBI

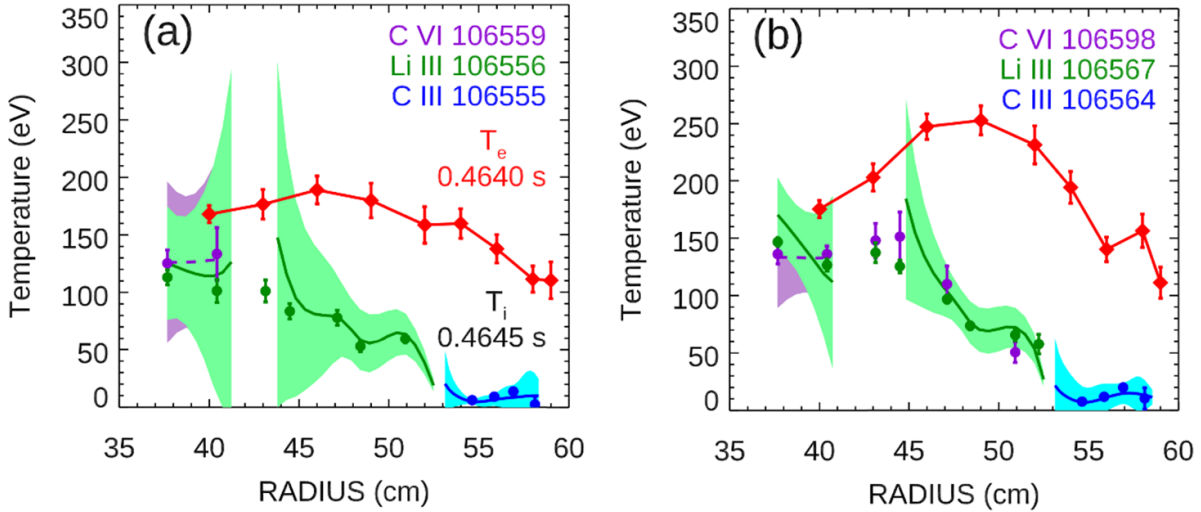


**Figure 14.** Line-integrated ‘apparent’ ion temperatures (points with error bars) from C VI (purple), Li III (green), and C III emission (blue); inverted local  $T_i$  profiles (splines with error bands); electron temperature profiles (red) from the (a) ohmic and (b) NBI-heated discharges in figure 13.

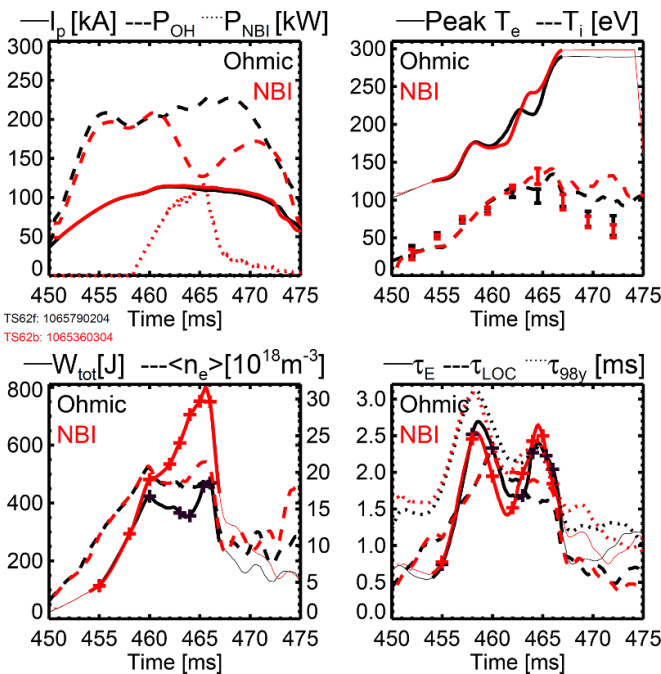


**Figure 15.** TRANSP and NUBEAM analysis of relatively flat temperature discharges in LTX- $\beta$  with low energy (13 keV) neutral beam injection (red), and a comparable ohmic discharge (black). Peak injected neutral beam power was  $\sim 290$  kW; the power indicated in the upper left panel (dotted line) is beam power coupled to the plasma, which is much lower than in the case shown in figure 11. Peak  $T_i$  data is from Li III Doppler broadening measurements.

heated discharge (right) relative to the ohmic discharge (left), similar in scale to the  $T_e$  increase. For the peaked  $T_e$  profile discharges, core  $T_i$  from C VI was used for the TRANSP runs in figure 11, while for the relatively flat  $T_e$  profile discharges, Li III was used in TRANSP for figure 15.

In figure 15 we show the results of TRANSP analysis for beam heating of targets with flat temperature profiles. Note the significant increase in the stored energy for beam heated discharges, despite modest coupled NBI power. The beam input power for these discharges was similar to the case shown in figures 12, 290 kW, with 45 kW of shine through. The largest loss of beam power is to the shell system, peaking initially at 175 kW, then dropping so that the power coupled to the plasma is  $\sim 100$  kW. As in figure 12, the TRANSP-calculated confinement times for both the beam heated and ohmic comparison discharges are notably similar.

## 5. Turbulence measurements

Theoretically, the use of lithium walls to produce high edge temperatures, reduce temperature gradients to negligible levels, and therefore eliminate thermal conduction, may limit energy losses to simple particle diffusion [45]. Reduction or elimination of the core temperature gradient could stabilize temperature gradient driven instabilities like the microtearing, electron temperature gradient, and ion temperature gradient modes (MTM, ETG, and ITG respectively). The remaining sources of instability drive include the density gradient and velocity space anisotropies due to trapped particles. Gyrokinetic simulations with the GYRO code for LTX predicted robust trapped electron mode (TEM) instability, and ITG was driven unstable during a simulated gas puff [45]. The TEM is a major contributor of the cross-field heat and particle transport [46], and a clear understanding of the TEM is vital to control the transport. Apart from the normalized ETG  $R/L_{Te}$ , the TEM threshold depends on several parameters such as the normalized density gradient  $R/L_n$ , safety factor  $q$ , and magnetic shear [47, 48]. Further, the TEM is predicted to be destabilized by decreased collisionality [46]. Because temperature gradient driven instabilities are minimized in the low recycling

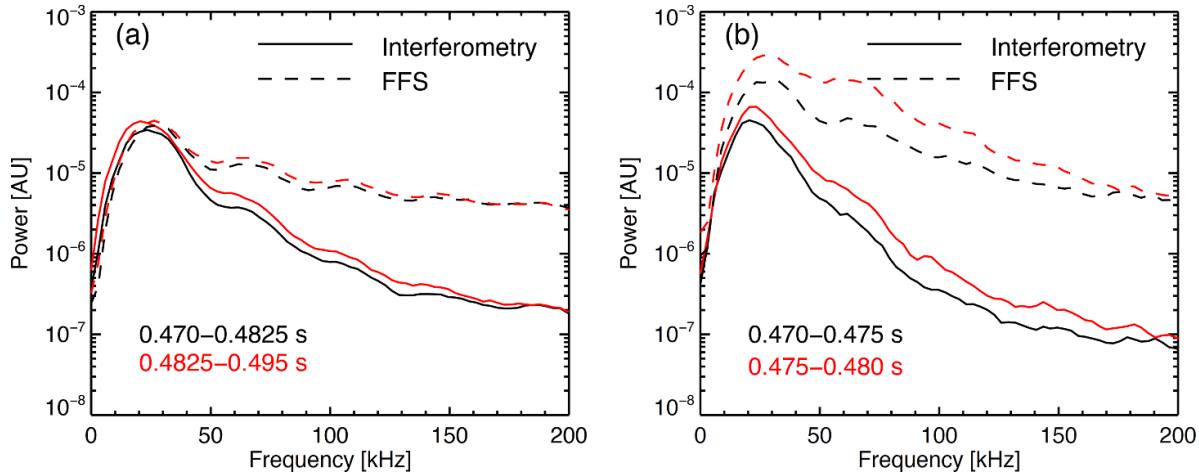


**Figure 16.** Fluctuation spectra from ohmic long current flattop discharges, using interferometry and FFS. (a) Averaged spectra from the low-density discharges in figure 8. Estimated  $\delta n/n$  from interferometry and FFS are  $\sim 0.02$  and  $\sim 0.03$ , respectively. (b) Averaged spectra from the high-density discharges in figure 9.  $\delta n/n$  from interferometry and FFS are  $\sim 0.02$  and  $\sim 0.06$ , respectively.

regime, LTX- $\beta$  offers a unique opportunity to document density gradient driven instabilities like the TEM in the low collisionality regime. To this end, the capability for electron density fluctuation measurements has been enhanced by the addition of two new diagnostics: the FFS diagnostic and the tunable fluctuation reflectometer.

### 5.1. FFS measurements

The FFS diagnostic utilizes the same hardware as the 288 GHz interferometer, and measures small-angle forward scattering along a radial view through the plasma [49]. While the interferometer is sensitive to  $0 \leq k_y < 0.7 \text{ cm}^{-1}$ , for FFS the  $e$ -folding sensitivity is shifted to the range  $0.4 < k_y < 1.7 \text{ cm}^{-1}$ . Here and below,  $k_y$  is the turbulence wavenumber in the transverse direction to the microwave beam axis. Future modifications will increase the upper limit to  $k_y \sim 3 \text{ cm}^{-1}$ . An example and comparison of both techniques is shown in figure 16, where the spectra of the fluctuation level  $\delta n/n$  are shown for ohmic long current flattop discharges previously shown in figures 8–10. Here the spectra from multiple shots have been averaged for two time periods (early and late), and the analysis begins at  $t = 470$  ms to avoid strong MHD. The raw signals are also high-pass filtered (15 kHz cutoff) to further reduce contamination from MHD and to emphasize the high frequency portion of the signal. For both the low density (figure 16(a)) and high density (figure 16(b)) cases, interferometry and FFS show fluctuations throughout the observed portion of the discharge. Fluctuation levels are smaller in the low density discharges, while in both cases  $\delta n/n$  is lowest early on and increases later in the discharge. The broader spectra for the FFS measurements are an indication that this diagnostic is sensing higher- $k$  turbulence compared to interferometry. Chord-averaged fluctuation levels from interferometry are  $\delta n/n \sim 0.02$  for both the low and high density cases, while the corresponding values from FFS are  $\delta n/n \sim 0.03$  and  $\sim 0.06$ .

### 5.2. Fluctuation reflectometry measurements

The tunable fluctuation reflectometer combines two fixed-frequency reflectometer channels (Ku-band: 13.1–20.5 GHz, Ka-band 20.3–40 GHz) with the vacuum interface for the existing profile reflectometer (13.1–33.5 GHz) [50]. Density coverage extends from 0.2 to  $1.4 \times 10^{13} \text{ cm}^{-3}$  for the profile reflectometer and to  $2 \times 10^{13} \text{ cm}^{-3}$  for the fluctuation reflectometer. The wavenumber sensitivity is centered at zero with an  $e$ -folding width of  $< 2.4 \text{ cm}^{-1}$ , corresponding to  $k_y \rho_s < 1.3$  for a typical discharge. The presence of both diagnostics on the same port allows for fluctuation measurements with wide temporal bandwidth (5 MHz), and high spatial resolution ( $< 1 \text{ cm}$ ). An example of this capability is shown in figures 17(a)–(f) where reflectometer data from representative ohmic long current discharges in figures 8–10 are presented. We note that for the high-density case from figure 9, the density profiles are steeper and the central portion of the reflectometer spectra are broader. In addition, these spectra show strong spatial variations and large asymmetries compared to the low-density case. Spectral asymmetries are typically associated with the Doppler effect due to turbulence propagation [51], while spectral broadening can occur due to changes in the turbulence characteristics such as fluctuation level, wavenumber spectrum, correlation length, etc [52]. Coupled with the higher  $\delta n/n$  measured by FFS and the steeper density gradient seen by the profile reflectometer, these fluctuation reflectometer spectra may indicate the destabilization of TEM-like turbulence during the latter phase of the high-density long current discharges. Future work will extend the gyrokinetic work from [45] to LTX- $\beta$  plasmas, utilizing full-wave codes for reflectometry and beam propagation codes for FFS to quantify the diagnostic response to turbulence. Finally, the variety and quantity of fluctuation data motivates the exploration of data parametrization methods to generate a database that can be used with data science techniques [53].

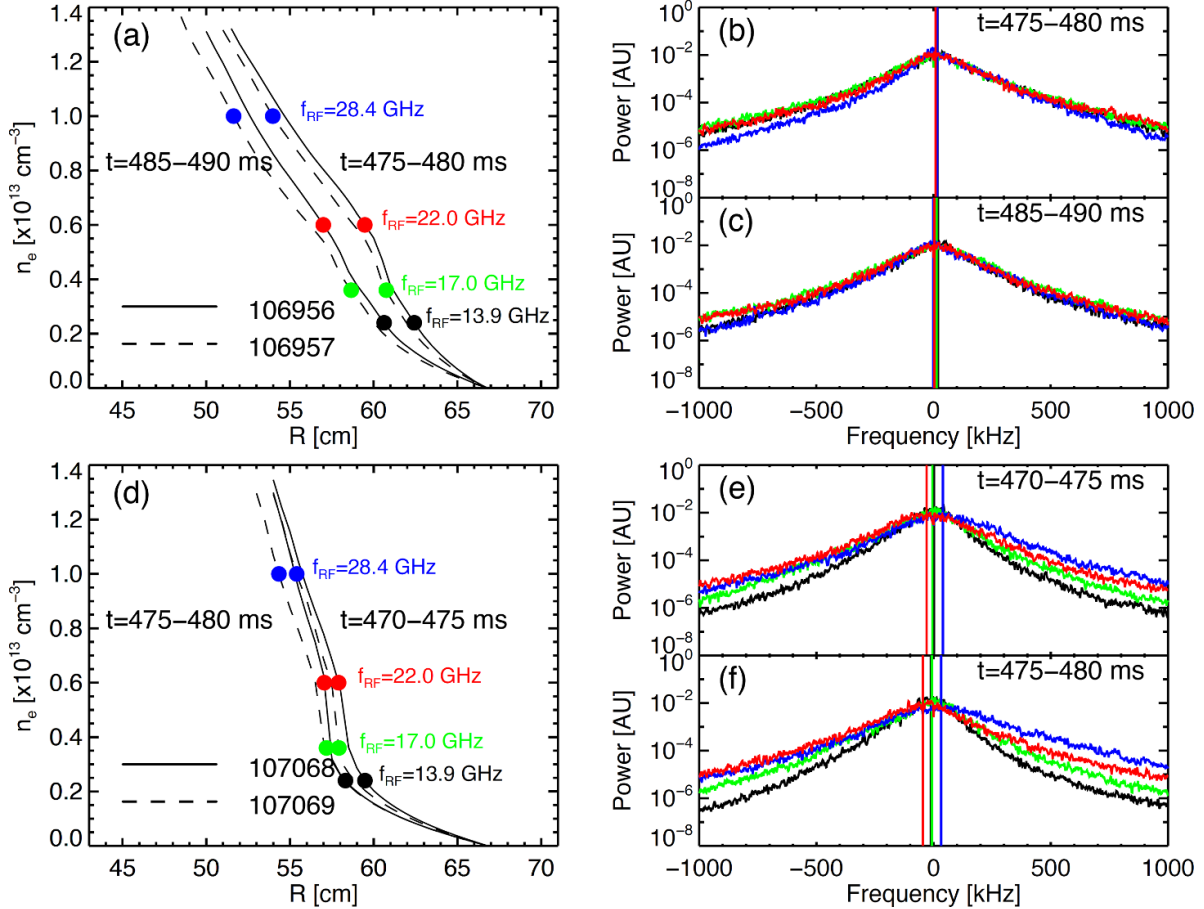


**Figure 17.** (a)–(c) Profile and fluctuation reflectometer measurements during the flat  $T_e$  phase for low density, long current discharges in figure 8. (a) Density profile and cutoff locations, (b) frequency spectrum of the fluctuation reflectometer signal during the early part of the flat  $T_e$  phase, and (c) the same analysis for the late portion. (d)–(f) Corresponding plots for high density, long current discharges in figure 9. The vertical lines in the spectra indicate the median frequency.

## 6. Summary, discussion, and future work

Careful control of the fueling of the discharge combined with repeated deposition of fresh lithium on all plasma facing surfaces in LTX- $\beta$  has produced flat electron temperature profiles which persist for several energy confinement times. The tokamak has presently been under vacuum, without a vent, for over 4 years, and recycling coefficients  $R < 0.5$  are consistently obtained. At this point, high recycling discharges are no longer available, even after extended periods without fresh lithium deposition. Flattened electron temperature profiles have been produced for central plasma densities up to  $2 \times 10^{19} \text{ m}^{-3}$ , with peaked density profiles. In contrast, peaked temperature profiles are still observed for the ions. The electron and ion profiles are expected to be decoupled, since the electron-ion energy exchange time for lower density discharges with flat electron temperature profiles is  $\sim 5\text{--}10$  ms, and the ions suffer charge exchange with the edge neutral population even with modest continuous edge fueling. For ohmic discharges, energy confinement times range up to 7–8 ms, which is  $\geq 2\times$  ITER H98y and Globus ST22 scalings. Confinement improves with density, as expected from Alcator LOC scaling for an ohmic tokamak, noting that measured energy confinement

times can be up to  $4\times$  greater than those predicted by the scaling.

Initial results with neutral beam heated discharges have also been obtained, with coupled beam power up to  $\sim 220$  kW, or modestly higher than the ohmic heating power, into higher density, strongly-fueled discharges with peaked electron temperature profiles (figures 10 and 11). Peak electron temperature is increased by an approximate factor of two with neutral beam heating. The edge temperature does not increase, so the peaking of the temperature profile increases with neutral beam heating in this case.

Discharges with relatively flat electron temperature profiles ( $T_{\text{edge}} \sim T_{\text{core}}/2$ ) have also been heated by neutral beam injection, although the lower density and increased electron temperature in these discharges increase the slowing down time of the injected ions on the electron population to 4–5 ms, comparable to the duration of neutral beam injection. For these discharges the increase in electron temperature with beam injection occurs broadly across the electron temperature profile, and the resultant temperature profile is broadened compared to the ohmic target (figure 13).

For both more peaked and relatively flat electron temperature profile scenarios, the energy confinement time with

beam heating is similar to the confinement time for the target ohmic discharge even though the total absorbed heating power approximately doubles. At the presently available levels of coupled beam power, there is no degradation of confinement time with auxiliary power.

Future modifications to the NBI system will enable increased heating power for longer duration to extend these confinement results toward regimes with dominant auxiliary heating and higher electron temperatures. Plans are to modify the vacuum vessel to increase the tangency radius of the neutral beam to  $R = 33$  cm in 2023, in order to reduce first orbit fast ion losses on the close-fitting shells for injection energies up to 17 keV. Higher injection energies will also allow the beam to operate at higher injected current and significantly higher power. Along with the re-aiming of the neutral beam, we plan to extend the beam pulse length to 20 ms to enable NBI heating of higher temperature plasmas with longer slowing down times. These upgrades and further optimization of beam and discharge parameters to improve fast ion confinement will also benefit future NBI fueling studies on LTX- $\beta$ . NBI fueling is potentially attractive for the high efficiency core fueling required for a low recycling fusion reactor [2, 15–17], though it is especially challenging in a modest scale device like LTX- $\beta$ .

Both the far-forward scattering and fluctuation reflectometry diagnostics are fully functional for monitoring broadband electron density fluctuations. FFS provides a chord-averaged view of fluctuations, while the measurement locations for fluctuation reflectometry are specified by the profile reflectometer. FFS and reflectometer measurements show several properties consistent with TEM turbulence during the latter portion of higher density gradient discharges. The frequency spectra of the reflectometer signals show strong variations in symmetry and width, indicating plasma flows and changes in the turbulence characteristics. Future work on LTX- $\beta$  will utilize access to very low recycling regimes in order to investigate the interplay between large variations in the electron density and temperature gradients, and the observed turbulence characteristics (e.g. ITG-like or TEM-like). A more complete analysis will require additional measurement capabilities (e.g.  $E \times B$  toroidal rotation velocity profiles from ion spectroscopy data—currently under development), in addition to gyrokinetic simulations and synthetic diagnostics.

## Acknowledgments

The authors acknowledge support from the entire past and present LTX- $\beta$  team, especially J. Armeli, D. Corl, T. Kozub, E. Merino, F. Rabanales, P. Sloboda, and G. Zimmer. The neutral beam was provided by TAE Technologies. This work was supported by U.S. Department of Energy under contract numbers DE-AC02-09CH11466, DE-AC05-00OR22725, DE-SC0019239, DE-AC52-07NA27344 and DE-SC0023481. The United States Government retains a non-exclusive, paid-up, irrevocable, world-wide license to publish or reproduce the published form of this manuscript,

or allow others to do so, for United States Government purposes. The digital data for this paper will be archived at <https://dataspace.princeton.edu/handle/88435/dsp01j6731612k>.

## ORCID iDs

- D.P. Boyle  <https://orcid.org/0000-0001-8091-8169>
- J. Anderson  <https://orcid.org/0000-0002-9644-5076>
- S. Banerjee  <https://orcid.org/0000-0003-0859-8855>
- R.E. Bell  <https://orcid.org/0000-0001-9544-498X>
- W. Capecchi  <https://orcid.org/0000-0002-0380-0180>
- D.B. Elliott  <https://orcid.org/0000-0003-4535-0381>
- C. Hansen  <https://orcid.org/0000-0001-6928-5815>
- S. Kubota  <https://orcid.org/0000-0003-1994-9825>
- B.P. LeBlanc  <https://orcid.org/0000-0003-1455-0129>
- A. Maan  <https://orcid.org/0000-0001-7474-2785>
- R. Maingi  <https://orcid.org/0000-0003-1238-8121>
- R. Majeski  <https://orcid.org/0000-0001-9437-0958>
- J.E. Menard  <https://orcid.org/0000-0003-1292-3286>
- T. Rhodes  <https://orcid.org/0000-0002-8311-4892>
- V. Soukhanovskii  <https://orcid.org/0000-0001-5519-0145>
- L. Zakharov  <https://orcid.org/0000-0002-2355-9144>

## References

- [1] Kaita R. 2019 Fusion applications for lithium: wall conditioning in magnetic confinement devices *Plasma Phys. Control. Fusion* **61** 113001
- [2] de Castro A., Moynihan C., Stemmley S., Szott M. and Ruzic D.N. 2021 Lithium, a path to make fusion energy affordable *Phys. Plasmas* **28** 050901
- [3] Apicella M.L., Mazzitelli G., Pericoli Ridolfini V., Lazarev V., Alekseyev A., Vertkov A. and Zagórski R. 2007 First experiments with lithium limiter on FTU *J. Nucl. Mater.* **363–365** 1346–51
- [4] Mansfield D.K. et al 1996 Enhancement of tokamak fusion test reactor performance by lithium conditioning *Phys. Plasmas* **3** 1892
- [5] Maingi R. et al 2011 Continuous improvement of H-mode discharge performance with progressively increasing lithium coatings in the national spherical torus experiment *Phys. Rev. Lett.* **107** 145004
- [6] Tabarés F.L., Oyarzabal E., Tafalla D., Martin-Rojo A.B., Alegre D. and de Castro A. 2015 First liquid lithium limiter biasing experiments in the TJ-II stellarator *J. Nucl. Mater.* **463** 1142–6
- [7] Zuo G.Z. et al 2020 Improvement on the plasma performances via application of flowing lithium limiters in EAST tokamak *Phys. Scr.* **T171** 014008
- [8] Ruzic D.N., Xu W., Andruczyk D. and Jaworski M.A. 2011 Lithium–metal infused trenches (LiMIT) for heat removal in fusion devices *Nucl. Fusion* **51** 102002
- [9] Puiatti M.E. et al 2013 Wall conditioning and density control in the reversed field pinch RFX-mod *Nucl. Fusion* **53** 073001
- [10] Chowdhuri M.B. et al 2013 Improvement of plasma performance with lithium wall conditioning in Aditya Tokamak *Plasma Sci. Technol.* **15** 123
- [11] Osborne T.H. et al 2015 Enhanced H-mode pedestals with lithium injection in DIII-D *Nucl. Fusion* **55** 063018
- [12] Guo H. et al 2015 Achieving a long-lived high-beta plasma state by energetic beam injection *Nat. Commun.* **6** 6897

- [13] Dunlea C., Xiao C. and Hirose A. 2021 Performance improvement with plasma edge biasing on SPECTOR *Phys. Plasmas* **28** 032506
- [14] Maingi R. *et al* 2019 Summary of the FESAC transformative enabling capabilities panel report *Fusion Sci. Technol.* **75** 167–77
- [15] Krasheninnikov S.I., Zakharov L.E. and Pereverzev G.V. 2003 On lithium walls and the performance of magnetic fusion devices *Phys. Plasmas* **10** 1678
- [16] Zakharov L.E., Gorelenkov N.N., White R.B., Krasheninnikov S.I. and Pereverzev G.V. 2004 Ignited spherical tokamaks and plasma regimes with LiWalls *Fusion Eng. Des.* **72** 149–68
- [17] White R.B. 2014 Chapter 10: the Lithium wall fusion concept *The Theory of Toroidally Confined Plasmas* 3rd edn (London: Imperial College Press) pp 447–56
- [18] Boyle D.P., Majeski R., Schmitt J., Hansen C., Kaita R., Kubota S., Lucia M. and Rognlien T. 2017 Observation of flat electron temperature profiles in the lithium tokamak experiment *Phys. Rev. Lett.* **119** 015001
- [19] Majeski R. *et al* 2017 Compatibility of lithium plasma-facing surfaces with high edge temperatures in the lithium tokamak experiment *Phys. Plasmas* **24** 056110
- [20] Elliott D. *et al* 2020 Initial results from the newly upgraded LTX- $\beta$  *IEEE Trans. Plasma Sci.* **48** 1382
- [21] Boyle D.P. *et al* 2021 Extending the low-recycling regime to higher performance discharges and liquid lithium walls in the lithium tokamak experiment- $\beta$  47th EPS Plasma Physics Conf. p P1.1023 (available at: <http://ocs.ciemat.es/EPS2021PAP/pdf/P1.1023.pdf>)
- [22] Majeski R. *et al* 2013 Particle control and plasma performance in the lithium tokamak experiment *Phys. Plasmas* **20** 056103
- [23] Berzak Hopkins L., Menard J., Majeski R., Lundberg D.P., Granstedt E., Jacobson C., Kaita R., Kozub T. and Zakharov L. 2012 Plasma equilibrium reconstructions in the lithium tokamak experiment *Nucl. Fusion* **52** 063025
- [24] Maan A. *et al* 2023 Improved neutral and plasma density control with increasing lithium wall coatings in the Lithium Tokamak Experiment- $\beta$  (LTX- $\beta$ ) *Nucl. Mater. Energy* **35** 101408
- [25] Lundberg D.P. 2012 Fueling studies on the lithium tokamak experiment *Ph D Dissertation* Princeton University (available at: <http://arks.princeton.edu/ark:/88435/dsp01mc87pq27c>)
- [26] Banerjee S. *et al* 2022 On the role of neutrals in achieving flat temperature profiles and exciting tearing mode activity in LTX- $\beta$  64th Annual Meeting of the APS Division of Plasma Physics (Spokane, Washington, 17–21 October) (available at: <https://meetings.aps.org/Meeting/DPP22/Session/CP11.2>)
- [27] Hawryluk R.J. 1980 An empirical approach to Tokamak transport *Physics of Plasmas Close to Thermonuclear Conditions* vol 1, ed B. Coppi *et al* (Brussels: CEC) pp 19–46 (available at: <https://transp.pppl.gov/files/Hawryluk.pdf>)
- [28] Breslau J. *et al* 2018 TRANSP. Computer software. USDOE Office of Science (SC) (Fusion Energy Sciences (FES)) (<https://doi.org/10.11578/dc.20180627.4>)
- [29] Boyle D.P. 2016 Measurements of impurity concentrations and transport in the lithium tokamak experiment *Ph D Dissertation* Princeton University (available at: <http://arks.princeton.edu/ark:/88435/dsp01fj236457r>)
- [30] Goldston R.J. 1984 Energy confinement scaling in Tokamaks: some implications of recent experiments with ohmic and strong auxiliary heating *Plasma Phys. Control. Fusion* **26** 87
- [31] ITER Physics Basis Expert Groups on Confinement and Transport and Confinement Modelling and Database, ITER Physics Basis Editors 1999 Chapter 2: plasma confinement and transport *Nucl. Fusion* **39** 2175
- [32] Kurskiv G.S. *et al* 2022 Energy confinement in the spherical tokamak Globus-M2 with a toroidal magnetic field reaching 0.8 T *Nucl. Fusion* **62** 016011
- [33] Kaye S.M., Connor J.W. and Roach C.M. 2021 Thermal confinement and transport in spherical tokamaks: a review *Plasma Phys. Control. Fusion* **63** 123001
- [34] Stangeby P. 2000 *The Plasma Boundary of Magnetic Fusion Devices* (New York: Taylor and Francis) (<https://doi.org/10.1201/9780367801489>)
- [35] Maan A. *et al* 2022 Low recycling, low collisionality and high performance with lithium conditioning in LTX- $\beta$  64th Annual Meeting of the APS Division of Plasma Physics (Spokane, Washington, 7–21 October) (available at: <https://meetings.aps.org/Meeting/DPP22/Session/UI01.3>)
- [36] Stotler D. and Karney C. 1994 Neutral gas transport modeling with DEGAS2 *Contrib. Plasma Phys.* **34** 392
- [37] Hansen C., Boyle D.P., Schmitt J.C. and Majeski R. 2017 Equilibrium reconstruction with 3D eddy currents in the lithium tokamak experiment *Phys. Plasmas* **24** 042513
- [38] Ivanov A.A. *et al* 2002 Diagnostic neutral beams for plasma studies in magnetic fusion devices 19th IAEA Fusion Energy Conf. (Lyon, France, 14–19 October 2002) (IAEA-CN-94), paper FT/P1-18 (available at: [www-pub.iaea.org/MTCD/publications/PDF/csp\\_019c/pdf/ftp1\\_18.pdf](http://www-pub.iaea.org/MTCD/publications/PDF/csp_019c/pdf/ftp1_18.pdf))
- [39] Hughes P., Capecchi W., Elliott D.B., Zakharov L.E., Bell R.E., Hansen C., Boyle D.P., Gorelenkov S.N., Majeski R. and Kaita R. 2021 Toroidal plasma acceleration due to NBI fast ion losses in LTX- $\beta$  *Plasma Phys. Control. Fusion* **63** 085020
- [40] Capecchi W., Anderson J.K., Boyle D.P., Hughes P.E., Maan A., Majeski R., Elliott D.B. and Hansen C. 2021 Neutral beam prompt loss in LTX- $\beta$  *Nucl. Fusion* **61** 126014
- [41] Pankin A., McCune D., Andre R., Bateman G. and Kritz A. 2004 The Tokamak Monte Carlo fast ion module NUBEAM in the national transport code collaboration library *Comput. Phys. Commun.* **159** 157–84
- [42] Elliott D.B. *et al* 2022 Expansion of the LTX-beta Thomson scattering system, including high-field side measurements with off-normal viewing angles 64th Annual Meeting of the APS Division of Plasma Physics (Spokane, Washington, 17–21 October) (available at: <https://meetings.aps.org/Meeting/DPP22/Session/CP11.5>)
- [43] Bell R.E. 2014 Development and operation of a high-throughput accurate-wavelength lens-based spectrometer *Rev. Sci. Instrum.* **85** 11E404
- [44] Bell R.E. 2021 Inversion technique to obtain local ion temperature profiles for an axisymmetric plasma with toroidal and radial velocities *Plasma Phys. Control. Fusion* **63** 045023
- [45] Granstedt E.M. 2013 The low recycling lithium boundary and implications for plasma transport *Ph D Dissertation* Princeton University (available at: <http://arks.princeton.edu/ark:/88435/dsp01xp68kg328>)
- [46] Banerjee S., Mordijk S., Barada K., Zeng L., Groebner R., Osborne T., Rhodes T.L., Snyder P.B., Grierson B. and Diallo A. 2021 Evolution of ELMs, pedestal profiles and fluctuations in the inter-ELM period in NBI- and ECH-dominated discharges in DIII-D *Nucl. Fusion* **61** 056008
- [47] Ryter F., Angioni C., Peeters A.G., Leuterer F., Fahrbach H.-U. and Suttrop W. 2005 Experimental study of trapped-electron-mode properties in tokamaks:

- threshold and stabilization by collisions *Phys. Rev. Lett.* **95** 085001
- [48] Kessel C., Manickam J., Rewoldt G. and Tang W.M. 1994 Improved plasma performance in tokamaks with negative magnetic shear *Phys. Rev. Lett.* **72** 1212
- [49] Kubota S., Majeski R., Boyle D.P., Kaita R., Kozub T., Lantsov R., Merino E., Nguyen X.V., Peebles W.A. and Rhodes T.L. 2018 Millimeter-wave interferometry and far-forward scattering for density fluctuation measurements on LTX- $\beta$  *Rev. Sci. Instrum.* **89** 10H114
- [50] Kubota S. et al 2017 A frequency-modulated continuous-wave reflectometer for the lithium tokamak experiment *Rev. Sci. Instrum.* **88** 053502
- [51] Hirsch M., Holzhauer E., Baldzuhn J., Kurzan B. and Scott B. 2001 Doppler reflectometry for the investigation of propagating density perturbations *Plasma Phys. Control. Fusion* **43** 1641
- [52] Nazikian R., Kramer G.J. and Valeo E. 2001 A tutorial on the basic principles of microwave reflectometry applied to fluctuation measurements in fusion plasmas *Phys. Plasmas* **8** 1840
- [53] Sun Y., Sabot R., Heuraux S., Garbet X., Hacquin S., Hornung G. and Verdoolaege G. 2019 Experimental trends of reflectometry frequency spectra emerging from a systematic analysis of the Tore Supra database *Phys. Plasmas* **26** 032307